POLITECNICO
MILANO 1863

DIPARTIMENTO DI MECCANICA

mecc

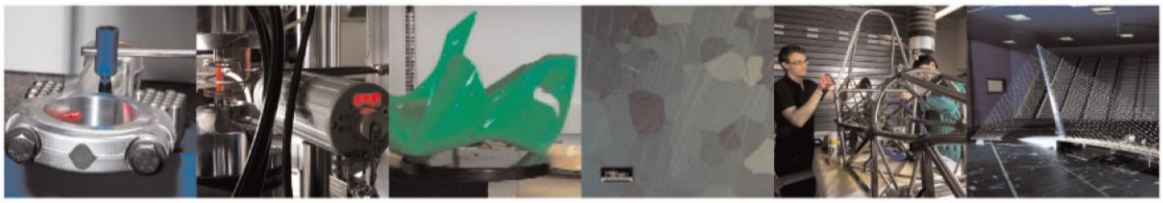

A tensor-based hierarchical process monitoring approach for anomaly detection in additive manufacturing

Yang, W, Grasso, M, Colosimo, BM, Paynabar, K.

DIPARTIMENTO DI MECCANICA ■ POLITECNICO DI MILANO
via G. La Masa, 1 ■ 20156 Milano ■ EMAIL (PEC): pecmecc@cert.polimi.it
http://www.mecc.polimi.it
Rev. 0

A Tensor-Based Hierarchical Process Monitoring Approach for Anomaly Detection in Additive Manufacturing

Wei Yang, Marco Grasso, Bianca Maria Colosimo, Kamran Paynabar

***Abstract*—Additive Manufacturing (AM) is a technology that enables the creation of complex shapes with advanced structural and functional properties. It has transformed the traditional manufacturing operations into a more flexible and efficient process, reshaping the whole value chain and allowing new levels of product customization. AM is a layer-by-layer manufacturing process, in which materials are deposited in each layer to create the object of interest. Due to the layer-wise nature of the process, anomalies and defects might occur within each layer, across several layers or throughout the whole sample. An accurate and responsive detection strategy that enables the detection of various types of anomalies is essential for ensuring the quality and integrity of the manufactured product. In this paper, a hierarchical in-situ process monitoring approach, namely, a three level monitoring strategy, is proposed to detect local, layer-wise and sample-wise anomalies using thermal videos acquired during the manufacturing process. The proposed approach integrates hierarchical low-rank tensor decomposition methods with statistical monitoring techniques to effectively detect anomalies at different levels, namely, the within-layer level, the layer level, and the sample level. Simulations are used to evaluate the performance of the method and compare with existing benchmarks. The proposed approach is also applied to thermal videos acquired during the laser powder bed fusion process to illustrate its effectiveness in practice.**

***Note to Practitioners*—The problem of this paper is motivated by the need to anticipate the detection of anomalies and defects while the part is being built, exploiting various possible sources of in-line data available in additive manufacturing processes. More precisely, this study deals with the problem of in-line and in-situ detection of process anomalies via infrared video imaging in laser powder bed fusion, a metal 3D printing process that enables very high accuracy, resolution and mechanical properties. Existing image-based monitoring approaches focus either on a frame-wise detection of anomalous patterns, where single frames are considered as random realizations of the process, or on spatio-temporal methods, where the temporal evolution of process patterns in consecutive frames is taken into account. However, real process anomalies may occur at different levels and on different scales, making existing methods suitable to detect just a reduced set of possible unstable states. To be specific, anomalies might occur within each layer, across the whole layer and throughout the entire sample. This study shows that the integration of frame-wise, layer-wise and sample-wise monitoring levels, which is referred to as hierarchical monitoring, represents an effective approach for anomaly detection in industrial applications where the type and severity of the anomaly are unpredictable. The performance of the proposed methods is examined under various noise levels and different anomaly scenarios, and compared against benchmark monitoring approaches. The results demonstrate the importance of adopting hierarchical process monitoring approach. In future research, its possible extensions to other industrial processes can be explored.**

***Index Terms*—Process Monitoring, Low-Rank Tensor Decomposition, Control Charts, Additive Manufacturing**

Wei Yang and Kamran Paynabar are with the H. Milton Stewart School of Industrial and Systems Engineering, Georgia Institute of Technology, Atlanta, GA 30332-0205 USA (e-mail: kamran.paynabar@isye.gatech.edu)

Marco Grasso and Bianca Maria Colosimo are with Dipartimento di Meccanica, Politecnico di Milano, Via La Masa 1, 20156, Italy

I. Introduction

Additive manufacturing (AM), also known as 3D printing, has seen increasing number of applications in the era of industry 4.0 due to its ability of creating new and complex shapes that overcomes the limits of traditional manufacturing processes and reshapes the whole value chain [1][2]. AM technologies also contribute to the digital and twin transition of the advanced manufacturing industry, thanks to new levels of data availability throughout the entire duration of the process. Such big data can be acquired by means of a variety of different sensors installed on AM systems exploiting the layer-by-layer production paradigm. Indeed, different from any other processes, quantities of interest can be measured in every layer, while the part is being produced, leading to brand new opportunities in terms of enhanced process and product qualification practices as well as new ways to reduce wastes and defects within the whole production process. A large and rapidly growing number of studies and industrial investments have been devoted to the development of data-driven solutions in this framework. A major field of research regards the use of in-line data coming from in-situ sensors to automatically detect process anomalies and the onsets of defects in the part. Methods in this field are commonly referred to as "in-situ process monitoring" [3][4][5][6]. A key driver for in-situ monitoring in AM is the ability to anticipate unstable and out-of-control states during the process rather then relying on costly and time-consuming post-process non-destructive tests. Combining this ability with reactive, adaptive or corrective actions could help one mitigate undesired part-to-part variations and keep defect rates compliant with stringent quality requirements. To this aims, the majority of studies in the literature has focused on the use of high-dimensional (HD) data streams, i.e., images or videos acquired with high spatial and/or high temporal resolution cameras in different wavelength ranges. Mainstream methods commonly aim to detect anomalies on a layer-by-layer basis (also referred to as "level 1" methods in Grasso et al. [4]) or anomalies occurring within the layer, during the production of the layer

(corresponding to "level 2" and "level 3" methods according to the classification in Grasso et al. [4]). In the former case, the anomaly can be detected once the production of the layer has been completed, implying a temporal scale that coincides with the sequence of layers. In the latter case, anomalies can be detected only if fast process dynamics are monitored with a high temporal resolution. This implies a much finer temporal scale, which corresponds to the frame rate of video-image data recording. A large portion of in-situ image- and video image-based process monitoring methods proposed in the AM literature involve the computation and analysis of pre-defined synthetic descriptors [7][4][3]. The selection of these descriptors is usually driven by engineering knowledge about the underlying process physics (e.g., melt pool size, number of spatters, time spent above a temperature threshold, etc.). Traditional process monitoring or classification techniques are then applied to these descriptors to determine the quality and stability of the process. Another category of methods investigated by several authors involve the use of deep neural networks [8][9][10][11][12][13]. They take advantage of big data streams commonly available in AM, and they avoid any ad-hoc selection of relevant descriptor. A third, and more restricted, category of methods includes statistical techniques used to model and synthesize the information content enclosed in video image streams via spatial, spatio-temporal or data reduction models [14][15][16]. They aim to overcome the information loss entailed in descriptor selection, avoiding at the same time a black box analytic framework.

Each of these in-situ monitoring methods in AM is commonly designed to detect one single type of process anomaly, occurring on one single level. Nevertheless, real anomalies may occur at different levels, i.e., they may generate within a small area of the layer, or they may introduce shifts in the measured quantities in one whole layer, or they can even affect one entire region of the build along many consecutive layers or the whole part. Process monitoring techniques designed to detect anomalies at one level may be not (or poorly) effective in the detection of anomalies on other levels. Moreover, it is not possible to predict in advance the type of anomaly or when it will occur, or how it will generate and propagate. This makes the use of one single monitoring tool suitable to detect only one subset of possible out-of-control states. The possibility to overcome this limitation motivated the present study. The underlying idea consists of monitoring the process by combining different spatial and temporal scales at which the information content enclosed in HD video-image data streams can be decomposed in low-dimensional (LD) spaces using tensor decomposition techniques. The resulting method is named "hierarchical process monitoring" approach, since out-of-control shifts (anomalies) can be searched for at different levels and on different scales. The aim is to expand the range of anomaly types that can be effectively identified, enhancing the flexibility of the process monitoring tool, while preserving the performances in terms of false positives and false negatives. It should be noted that the applications of the proposed hierarchical process monitoring approach goes beyond AM. Generally speaking, the proposed approach may be used for monitoring processes whose multi-level variability is measured by HD data streams. As an example, in batch processes, anomalies may affect the process behaviour within the batch, its variability from batch to batch or from part to part. In this case, a hierarchical monitoring approach may enhance the detection of anomalies, thanks to a multi-level representation of the information extracted from monitored data.

As mentioned earlier, the proposed approach is applied to video-image data streams. Generally speaking, a video-image data stream represents a HD data format, where intensity (color), spatial and temporal scales shall be preserved to capture and model the relevant information content [17]. A suitable framework to deal with this type of data regards the use of tensor statistics. The proposed approach belongs to this framework. Various tensor-based process monitoring methods have been proposed so far [18][19]. In [20], an image-based process monitoring approach has been developed by treating the collections of image frames as a tensorial object. Yan et al. [20] used the tensor rank-one decomposition approach to extract monitoring features, under the assumption of a stationary process. In order to deal with more challenging applications where the process pattern in video frames is non-stationary, as it occurs in the application considered in this study, Yan et al. [21] proposed a spatio-temporal smooth sparse decomposition to separate anomalies, in the form of abrupt changes, from the natural spatio-temporal structure. Variants of the method were also developed and applied in AM to detect specific types of process anomaly, i.e., so-called hot-spot events [15], or melt pool anomalies [22]. Such tensor-based methods are quite effective in the detection of spatial anomalies in one frame and/or spatio-temporal anomalies in a sequence of frames. However, they still rely on the classical paradigm where the method is suitable to detect just a specific type of anomalies (as in [15] or in [22]) or anomalies occurring on a specific level or scale (i.e., intensity shifts among pixels or pattern changes among frames).

The main contribution of this paper is to introduce a different and novel perspective in the use of tensor-based methods. Indeed, the proposed idea consists of using the tensor decomposition, more specifically the Tucker decomposition [23], not only to monitor the process within a lower dimensional space, but also to decompose the whole information on different scales, leading to multiple levels at which sensor data can be processed and monitored. The resulting process monitoring perspective is "hierarchical" in nature, because the monitoring levels can be hierarchically ordered from the local to the global scale. This allows dealing with process monitoring applications where the nature and variety of anomalies go beyond the limitations mentioned above. In the AM application that motivates this study, these levels consist of events that may occur within one single layer, layer-wise (i.e., from one layer to another) and sample-wise (i.e., from one sample, or part, to another). Thanks to the hierarchical monitoring framework, it is therefore possible to detect a wide variety of out-of-control events, from very local and spatially-clustered ones (typically characterized also by a fast temporal dynamic), to phenomena that have a more global effect, causing process shifts on a slower and longer term scale. By simultaneously

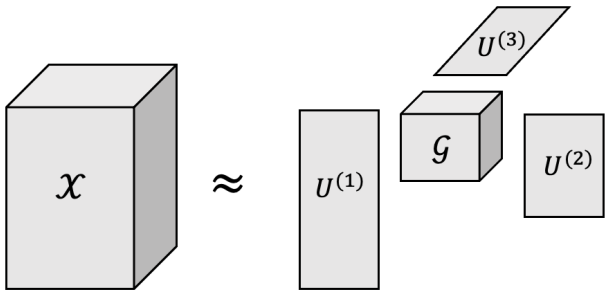

Fig. 1. The illustration of Tucker decomposition of rank-3 tensor

monitoring the process at these different levels, a broader variety of possible anomalies can be effectively detected, with the advantage of using one single hierarchical data modeling and monitoring framework, instead of combining several ad-hoc statistical tools.

The proposed monitoring approach is applied to laser powder bed fusion (L-PBF) [24], the most largely adopted metal AM technology for highly complex parts. Infrared videos capturing the laser-material interaction and the thermal history within multiple layers and different parts have been used as data source for in-line and in-situ anomaly detection. As the process entails a local melting and fast solidification of the material, thermal video imaging in the infrared range provides a rich information content about most relevant heating and cooling patterns, which are strongly connected to the possible onset of process defects. Additionally, the effectiveness of the methodology was tested using simulated data. Its performance was compared against different benchmark methods and in the presence of different noise levels in the input video-image data.

Section 2 introduces the tensor notation and multilinear algebra the proposed approach grounds on. In Section 3, the proposed tensor-based hierarchical process monitoring methodology is presented. Section 4 presents the simulation study and comparison with benchmark methods. Section 5 focuses on the case study and the achieved results. Section 6 concludes the paper.

II. Tensor Notation and Multilinear Algebra

In this section, we introduce basic notations, definitions and operators in tensor analysis. Throughout this paper, we denote scalars and vectors by lowercase letters, e.g., x and boldface lowercase letters, e.g., $\boldsymbol{x}$ respectively. Matrices and tensors are denoted by boldface uppercase letters, e.g., $\boldsymbol{U}$ and calligraphic letters $\mathcal{X}$ respectively. An N_{th} order tensor is represented by $\mathcal{X} \in \mathbb{R}^{I_1 \times I_2 \times \ldots I_N}$, where I_k denotes the number of elements in the k^{th} dimension. A rank one tensor can be produced by extending the concept of vector outer product to tensor product for N vectors. For example, an N-way tensor of rank one can be represented by $\mathcal{X} = \boldsymbol{a}^{(1)} \circ \boldsymbol{a}^{(2)} \circ \cdots \cdot \boldsymbol{a}^{(N)}$ where the $\boldsymbol{a}^{(k)}$ is the a vector of dimension I_k. The rank of a tensor $\mathcal{X}$ is defined as the smallest number of rank-one tensors whose sum can generate $\mathcal{X}$. Tensor matricization is the operation which unfolds or flattens an N-way tensor into a matrix. Mode-n matricization of a tensor $\mathcal{X} \in \mathbb{R}^{I_1 \times I_2 \times \ldots I_N}$ is denoted by $\boldsymbol{X}_{(k)} \in \mathbb{R}^{I_1 \times (I_1 \cdot I_2 \cdot \ldots \cdot I_N)}$ whose columns are the mode-n vectors. The Kronecker product of matrices $\boldsymbol{A} \in \mathbb{R}^{I \times J}$ and $\boldsymbol{B} \in \mathbb{R}^{K \times L}$ is denoted by $\boldsymbol{A} \otimes \boldsymbol{B}$, which is a matrix of size $(IK) \times (JL)$:

$$\boldsymbol{A} \otimes \boldsymbol{B} = \begin{bmatrix} a_{11}\boldsymbol{B} & \cdots & a_{1L}\boldsymbol{B} \\ \vdots & \ddots & \vdots \\ a_{K1}\boldsymbol{B} & \cdots & a_{KL}\boldsymbol{B} \end{bmatrix}.$$

The Khaoti-Rao Product between two matrices $\boldsymbol{A} \in \mathbb{R}^{I \times K}$ and $\boldsymbol{B} \in \mathbb{R}^{J \times K}$ is denoted by $\boldsymbol{A} \odot \boldsymbol{B}$, is a matrix of size $(IJ) \times K$ and defined by the column-wise Kronecker product:

$$\boldsymbol{A} \odot \boldsymbol{B} = \begin{bmatrix} \boldsymbol{a}_1 \otimes \boldsymbol{b}_1 & \boldsymbol{a}_2 \otimes \boldsymbol{b}_2 & \boldsymbol{a}_2 \otimes \boldsymbol{b}_2 \end{bmatrix}.$$

The k-mode product of a tensor $\mathcal{X} \in \mathbb{R}^{I_1 \times I_2 \times \ldots I_N}$ by a matrix $\boldsymbol{U} \in \mathbb{R}^{J \times I_k}$ is a defined as $(\mathcal{X} \times_k \boldsymbol{U})_{i_1, i_2, \cdots, i_{k-1}, j, i_{k+1}, \cdots, i_N} = \sum_{i_k=1}^{I_k} \mathcal{X}_{i_1, \cdots, i_k, \cdots, i_N} \boldsymbol{U}_{j, i_k}$. The Frobenius norm of a tensor $\mathcal{X} \in \mathbb{R}^{I_1 \times I_2 \times \ldots I_N}$ is defined as tensor scalar product of $\mathcal{X}$ with itself: $\|\mathcal{X}\|_F = \sqrt{\langle \mathcal{X}, \mathcal{X} \rangle} = \sqrt{\sum_{i_1} \cdots \sum_{i_N} \mathcal{X}_{i_1, i_2, \cdots, i_N} \mathcal{X}_{i_1, i_2, \cdots, i_N}}$.

The CP decomposition decomposes a tensor as a sum of rank-one tensors. The decomposition of a tensor $\mathcal{X} \in \mathbb{R}^{I_1 \times I_2 \times \ldots I_N}$ can be represented as $\mathcal{X} \approx \sum_{r=1}^{R} \lambda_r a_r^{(1)} \circ a_r^{(2)} \circ \cdots \circ a_r^{(N)}$ with $\|a_r^{(i)}\| = 1$; $i = 1, 2, \cdots, N$.

The Tucker decomposition decomposes a tensor $\mathcal{X} \in \mathbb{R}^{I_1 \times I_2 \times \ldots I_N}$ into a core tensor $\mathcal{C} \in \mathbb{R}^{Q_1 \times Q_2 \times \cdots Q_N}$ and a set of factorizing matrix along each mode (see Figure 1), which can be defined as $\mathcal{X} = \mathcal{C} \times_1 \boldsymbol{U}^{(1)} \times_2 \boldsymbol{U}^{(2)} \cdots \boldsymbol{U}^{(N)}$ where each factorizing matrix $\boldsymbol{U}^{(k)} \in \mathbb{R}^{I_k \times Q_k}$. The core tensor with the ability of capturing interaction among different modes is considered as compressed version of the original tensor as often $Q_k < I_k$ $k = (1, 2, \cdots, N)$.

III. The Hierarchical Monitoring approach applied to AM

The underlying idea of the proposed hierarchical monitoring approach consists of decomposing the process monitoring problem at different temporal and spatial scales. In the AM application presented in this study, such scales include the within-layer, the between-layer and the between-sample scales. When process monitoring is designed and applied on one single scale, its anomaly detection power may considerably vary depending on the nature of the occurred anomaly. As an example, an alarm rule designed to signal a variation from one layer to another may be not effective in detecting an anomaly that affects a small portion of one single layer. Without prior information about the nature, extension and propagation mode of the anomaly, traditional process monitoring methods may be effective only for a restricted subset of out-of-control states. The idea behind the proposed hierarchical monitoring approach is precisely to overcome such limitation, enhancing the flexibility of the anomaly detection capability while preserving the performances in terms of false positives and false negatives. Figure 2 shows a general scheme of the proposed hierarchical methodology applied to the anomaly detection problem in the L-PBF process. It integrates tensor analysis with statistical process monitoring at three different levels to

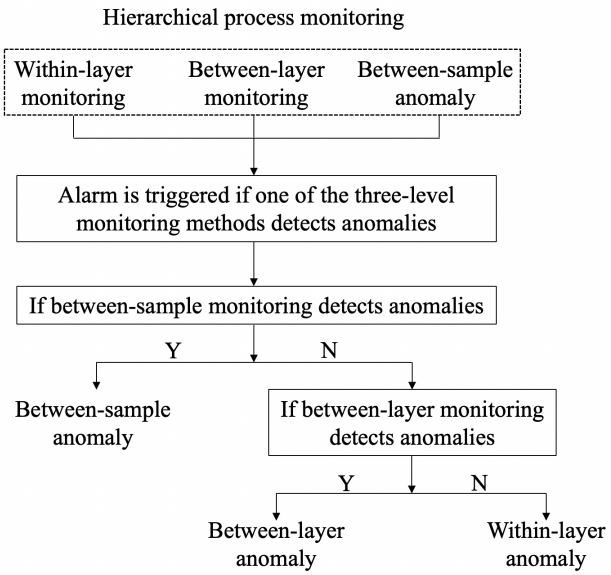

Fig. 2. General scheme of the proposed hierarchical process monitoring applied to the L-PBF process

detect anomalies in each of the three levels. If at least one of the three monitoring tools raises an alarm, a conclusion that an anomaly has occurred in the process can be drawn. Moreover, being a hierarchical method, diagnostic information about the nature of the occurred anomaly may be gathered as well, as shown in Figure 2. Indeed, depending on which monitoring tool has raised an alarm, it is possible to label the detected anomaly accordingly. In the subsequent sections, we elaborate this tensor-based hierarchical process monitoring approach.

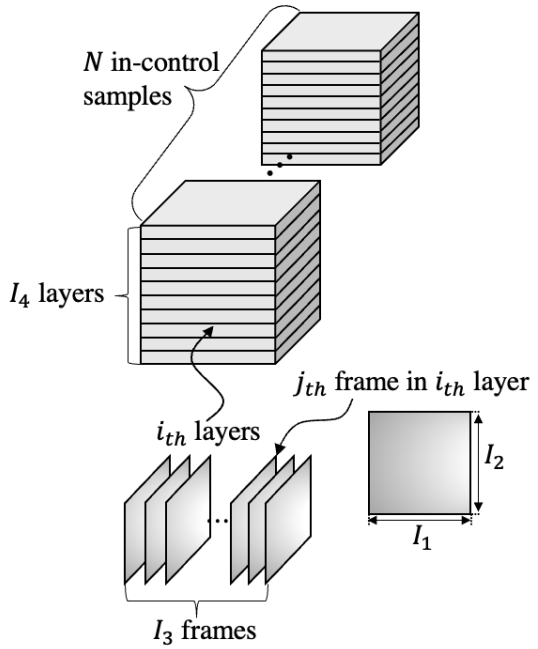

Fig. 3. Pictorial representation of the dimensions of the N in-control samples

A. Dimension Reduction using Tensor Decomposition

As mentioned earlier, video streams are used to monitoring the process at different levels. One particular challenge in dealing with video streams is high-dimensionality that impact the detection of any monitoring approaches. However, since the essential information of the video streams lies in a low-dimensional space, an effective dimension reduction method such as low-rank recovery approaches will help extract important feature for process monitoring. Specifically, due to the tensor structure of the video streams, we utilize Tucker decomposition to extract multi-resolution monitoring features.

Suppose N in-control samples of dimension $I_1 \times I_2 \times I_3 \times I_4$ are available for training (phase I analysis), where $I_1 \times I_2$ is the size of each image frame, I_3 is the number of frames captured for monitoring each layer, and I_4 is the number of layers in each sample (part). See Figure 3 for pictorial representation of the samples. We first use Tucker decomposition to learn the low-rank in-control structure of the data and extract the core tensors of the $i_{th}; i = 1, 2, \cdots, I_4$ layer, the $j_{th}; j = 1, 2, \cdots, I_3$ frame in the i_{th} layer, and the $k_{th}; k = 1, 2, \cdots, N$ sample for between layer monitoring, within layer monitoring and between sample monitoring, respectively. In addition, we demonstrate how to extract monitoring features for an incoming sample at the online monitoring stage using the low-rank structure recovered from the N in-control samples. Tucker decomposition decomposes a tensor into a set of basis matrices and a low-dimensional core tensor. As it offers more flexibility in comparison with CP decomposition where the core tensor is restricted to be diagonal, we utilize it for feature extractions.

1) Between-layer Monitoring: Between-layer monitoring strategy aims to monitor the printing process at the layer level. In AM process monitoring using thermal cameras, the creation of each layer is monitored by a sequence of image frames. We denote this sequence of images as $\mathcal{X} \in \mathbb{R}^{I_1 \times I_2 \times I_3}$. The first and second dimensions, I_1 and I_2, correspond to the width and height of a single image frame respectively. The third dimension I_3 corresponds to the number of frames recorded for printing one layer. Then, given N in-control samples for the i_{th} layer, we learn the basis matrices and the core tensors using the following optimization for Tucker decomposition:

$$\hat{\mathcal{G}}_i^{(k)}, \hat{\boldsymbol{A}}_i, \hat{\boldsymbol{B}}_i, \hat{\boldsymbol{C}}_i = \underset{\mathcal{G}_i^{(k)}, \boldsymbol{A}_i, \boldsymbol{B}_i, \boldsymbol{C}_i}{\operatorname{argmin}} \sum_{k=1}^{N} \|\mathcal{X}_k - \sum_{p=1}^{R_1} \sum_{q=1}^{R_2} \sum_{r=1}^{R_3} g_{i_{pqr}}^{(k)} \boldsymbol{a}_{i_p} \circ \boldsymbol{b}_{i_q} \circ \boldsymbol{c}_{i_r} \|_F^2$$

$$= \underset{\mathcal{G}_i^{(k)}, \boldsymbol{A}_i, \boldsymbol{B}_i, \boldsymbol{C}_i}{\operatorname{argmin}} \sum_{k=1}^{N} \|\mathcal{X}_k - [\![\mathcal{G}_i^{(k)}; \boldsymbol{A}_i, \boldsymbol{B}_i, \boldsymbol{C}_i]\!]\|_F^2 \quad (1)$$

Subject to $\mathcal{G}_i^{(k)} \in \mathbb{R}^{R_1 \times R_2 \times R_3}$, $\boldsymbol{A}_i \in \mathbb{R}^{I_1 \times R_1}$, $\boldsymbol{B}_i \in \mathbb{R}^{I_2 \times R_2}$, $\boldsymbol{C}_i \in \mathbb{R}^{I_3 \times R_3}$ and columnwise orthogonality for $\boldsymbol{A}_i, \boldsymbol{B}_i, \boldsymbol{C}_i$ where $\hat{\mathcal{G}}_i^{(k)}$ is the core tensor extracted for the sample $\mathcal{X}_k$; $k = 1, 2, \cdots, N$, $g_{i_{pqr}}^{(k)}$ is the $(p, q, r)_{th}$ element of $\mathcal{G}_i^{(k)}$, $\hat{\boldsymbol{A}}_i, \hat{\boldsymbol{B}}_i, \hat{\boldsymbol{C}}_i$ are the learned basis matrices and $\boldsymbol{a}_{i_p}$, $\boldsymbol{b}_{i_q}$ and $\boldsymbol{c}_{i_r}$ denote the p_{th}, q_{th} and r_{th} column of the basis matrices $\boldsymbol{A}_i$, $\boldsymbol{B}_i$ and $\boldsymbol{C}_i$, respectively.

In order to solve Problem 1 more efficiently, one can concatenate the samples and create a new tensor with higher order. Specifically, the tensor $\mathcal{X}_k$ of order 3 is transformed to $\mathcal{Y} \in \mathbb{R}^{I_1 \times I_2 \times I_3 \times N}$, where the last order corresponds to the samples. This is shown in the following proposition.

Proposition 1: Let $\mathcal{Y} \in \mathbb{R}^{I_1 \times I_2 \times I_3 \times N}$ denote the tensor of N in-control samples $\mathcal{X}_k$; $k = 1, 2, \cdots, N$. The basis matrices $\hat{\boldsymbol{A}}_i$, $\hat{\boldsymbol{B}}_i$ and $\hat{\boldsymbol{C}}_i$ obtained through Tucker decomposition of $\mathcal{Y}$ are the same solutions to (1) and $\sum_{l=1}^{R_4} \hat{d}_{i_l}^{(k)} \times \hat{s}_{i_{pqrl}} = \hat{g}_{i_{pqr}}^{(k)}$ where $\hat{d}_{i_l}^{(k)}$ is the $(k,l)_{th}$ element of $\hat{\boldsymbol{D}}_i$ and $\hat{s}_{i_{pqrl}}$ is the $(p,q,r,l)_{th}$ element of $\hat{\mathcal{S}}_i$

$$\hat{\mathcal{S}}_i, \hat{\boldsymbol{A}}_i, \hat{\boldsymbol{B}}_i, \hat{\boldsymbol{C}}_i, \hat{\boldsymbol{D}}_i = \underset{\mathcal{S}_i, \boldsymbol{A}_i, \boldsymbol{B}_i, \boldsymbol{C}_i, \boldsymbol{D}_i}{\operatorname{argmin}} \|\mathcal{Y} - \sum_{p=1}^{R_1}\sum_{q=1}^{R_2}\sum_{r=1}^{R_3}\sum_{l=1}^{R_4} s_{i_{pqrl}} \boldsymbol{a}_{i_p} \circ \boldsymbol{b}_{i_q} \circ \boldsymbol{c}_{i_r} \circ \boldsymbol{d}_{i_l}\|_F^2$$
$$= \underset{\mathcal{S}_i, \boldsymbol{A}_i, \boldsymbol{B}_i, \boldsymbol{C}_i, \boldsymbol{D}_i}{\operatorname{argmin}} \|\mathcal{Y} - [\![\mathcal{S}_i; \boldsymbol{A}_i, \boldsymbol{B}_i, \boldsymbol{C}_i, \boldsymbol{D}_i]\!]\|_F^2 \quad (2)$$

Subject to $\mathcal{S}_i \in \mathbb{R}^{R_1 \times R_2 \times R_3 \times R_4}$, $\boldsymbol{A}_i \in \mathbb{R}^{I_1 \times R_1}$, $\boldsymbol{B}_i \in \mathbb{R}^{I_2 \times R_2}$, $\boldsymbol{C}_i \in \mathbb{R}^{I_3 \times R_3}$, $\boldsymbol{D}_i \in \mathbb{R}^{N \times R_4}$ and columnwise orthogonality for $\boldsymbol{A}_i, \boldsymbol{B}_i, \boldsymbol{C}_i, \boldsymbol{D}_i$ where $\boldsymbol{D}_i$ is the basis matrix corresponding to the sample dimension, $\hat{\mathcal{S}}_i$ is the core tensor extracted.

Proof is given in Appendix A. The solutions to (2), can be obtained by using the alternating least square (ALS) algorithm [23].

The low-dimensional core tensor, $\mathcal{G}_i$, can be used as a set of features for monitoring layer i. Assuming that the underlying distribution of extracted features is tensor normal distribution, i.e., $\mathcal{G}_i \sim N(\mu_{\mathcal{G}_i}, \boldsymbol{\Sigma}_1, \boldsymbol{\Sigma}_2, \boldsymbol{\Sigma}_3)$, where $\mu_{\mathcal{G}_i}$ is the core tensor mean, and $\boldsymbol{\Sigma}_i$ is the covariance matrix along mode i, one can use a T^2 monitoring statistic and its corresponding control limit [25] given the mean and covariance matrices as discussed in Section B.

However, for online monitoring, the core tensor features should be extracted for each incoming sample. This is accomplished by using the low-dimensional basis matrices learned from the training phase, i.e., $\hat{\boldsymbol{A}}_i, \hat{\boldsymbol{B}}_i, \hat{\boldsymbol{C}}_i$ using the N in-control samples. Specifically, the core tensor for layer i of a new sample, $\mathcal{X}_m$, is obtained by the following optimization:

$$\tilde{\mathcal{G}}_i^{(m)} = \underset{\mathcal{G}_i^{(m)}}{\operatorname{argmin}} \|\mathcal{X}_m - \sum_{p=1}^{R_1}\sum_{q=1}^{R_2}\sum_{r=1}^{R_3} g_{i_{pqr}}^{(m)} \hat{\boldsymbol{a}}_{i_p} \circ \hat{\boldsymbol{b}}_{i_q} \circ \hat{\boldsymbol{c}}_{i_r}\|_F^2$$
$$= \underset{\mathcal{G}_i^{(m)}}{\operatorname{argmin}} \|\mathcal{X}_m - [\![\mathcal{G}_i^{(m)}; \hat{\boldsymbol{A}}_i, \hat{\boldsymbol{B}}_i, \hat{\boldsymbol{C}}_i]\!]\|_F^2 \quad (3)$$

where $\tilde{\mathcal{G}}_i^{(m)} \in \mathbb{R}^{R_1 \times R_2 \times R_3}$ is the extracted core tensor for the new sample $\mathcal{X}_m$.

Proposition 2: Given $\hat{\boldsymbol{A}}_i, \hat{\boldsymbol{B}}_i, \hat{\boldsymbol{C}}_i$, the core tensor $\mathcal{G}_i^{(m)}$ in (3) has a closed-form solution:

$$\tilde{\mathcal{G}}_i^{(m)} = \mathcal{X}_m \times_1 \hat{\boldsymbol{A}}_i^T \times_2 \hat{\boldsymbol{B}}_i^T \times_3 \hat{\boldsymbol{C}}_i^T \quad (4)$$

Proof is given in Appendix B.

Then, monitoring the i_{th} layer of an incoming sample is essentially to monitor the core tensor $\tilde{\mathcal{G}}_i^{(m)}$ under the assumption that core tensor comes from a tensor normal distribution with the estimated mean and covariance matrices, i.e., $\tilde{\mathcal{G}}_i^{(m)} \sim N(\bar{\mathcal{G}}_i^{(m)}, \hat{\boldsymbol{\Sigma}}_1^{(m)}, \hat{\boldsymbol{\Sigma}}_2^{(m)}, \hat{\boldsymbol{\Sigma}}_3^{(m)})$ or equivalently $vec(\tilde{\mathcal{G}}_i^{(m)}) \sim N(vec(\bar{\mathcal{G}}_i^{(m)}), \hat{\boldsymbol{\Sigma}}_3^{(m)} \otimes \hat{\boldsymbol{\Sigma}}_2^{(m)} \otimes \hat{\boldsymbol{\Sigma}}_1^{(m)})$, where $\bar{\mathcal{G}}_i^{(m)}$ is the core tensor mean and $\hat{\boldsymbol{\Sigma}}_i^{(m)}$ is the covariance matrix along mode i. The details on estimation and control limits are discussed in Section B.

2) Within-layer Monitoring: The within-layer monitoring strategy monitors the printing process at the frame level. We denote frame j in layer i of sample v as $\mathcal{F}_{ijv} \in \mathbb{R}^{I_1 \times I_2}$; $v = 1, 2, \cdots, N$. The first and second dimensions, I_1 and I_2, correspond to the width and height of the image frame, respectively. Performing Tucker decomposition on each frame is computationally expensive due to the large number of the frames. As a sequence of frames form a layer, it can be assumed that layer i and its corresponding frames share the same basis matrices. Therefore, we utilize the basis vectors learnt from the between-layer monitoring (i.e., Eq. 2) and try to learn a set of low-dimensional frame features that captures frame variability by solving the following optimization:

$$\hat{\mathcal{H}}_{ij}^{(v)} = \underset{\mathcal{G}_{ij}^{(v)}}{\operatorname{argmin}} \sum_{v=1}^{N} \|\mathcal{F}_{ijv} - \sum_{p=1}^{R_1}\sum_{q=1}^{R_2}\sum_{l=1}^{R_3} (h_{ij_{pql}}^{(v)} \times \hat{c}_{i_{jl}}) \hat{\boldsymbol{a}}_{i_p} \circ \hat{\boldsymbol{b}}_{i_q}\|_F^2 \quad (5)$$

where $\hat{c}_{i_{jl}}$ is a scalar which corresponds to $(j,l)_{th}$ element of the learnt basis matrix $\hat{\boldsymbol{C}}_i$ from between-layer monitoring, $\hat{\mathcal{H}}_{ij}^{(v)} \in \mathbb{R}^{R_1 \times R_2 \times R_3}$ is the extracted core tensor for $\mathcal{F}_{ijv}$; $v = 1, 2, \cdots, N$, and $h_{ij_{pql}}^{(v)}$ is the $(p,q,l)_{th}$ element of $\mathcal{H}_{ij}^{(v)}$.

Proposition 3: Given $\hat{\boldsymbol{A}}_i, \hat{\boldsymbol{B}}_i, \hat{\boldsymbol{C}}_i$, the closed form solution to (5) is:

$$vec(\hat{\mathcal{H}}_{ij}^{(v)}) = [\hat{\boldsymbol{A}}_i \otimes \hat{\boldsymbol{B}}_i \otimes \hat{\boldsymbol{c}}_{i_j}]^\dagger vec(\mathcal{F}_{ijv}) \quad (6)$$

where $\boldsymbol{M}^\dagger = (\boldsymbol{M}^T\boldsymbol{M})^{-1}\boldsymbol{M}^T$. The proof is given in Appendix C. These core tensors are used as monitoring features to set up the within-layer control charts and estimate its necessary parameters, i.e., the mean, covariance matrices and the control limit.

Similarly, we can determine the core tensor for the i_{th} layer and the j_{th} frame of a new sample, $\mathcal{F}_{ijl} \in \mathbb{R}^{I_1 \times I_2}$ using following optimization:

$$\tilde{\mathcal{H}}_{ij}^{(l)} = \underset{\mathcal{H}_{ij}^{(l)}}{\operatorname{argmin}} \|\mathcal{F}_{ijl} - \sum_{p=1}^{R_1}\sum_{q=1}^{R_2}\sum_{l=1}^{R_3} (h_{ij_{pql}}^{(l)} \times \hat{c}_{i_{jl}}) \hat{\boldsymbol{a}}_{i_p} \circ \hat{\boldsymbol{b}}_{i_q}\|_F^2 \quad (7)$$

where $\tilde{\mathcal{H}}_{ij}^{(l)} \in \mathbb{R}^{R_1 \times R_2 \times R_3}$ is the extracted core tensor for $\mathcal{F}_{ijl}$. Following from proposition 3, the solution to (7) is given by $vec(\tilde{\mathcal{H}}_{ij}^{(l)}) = [\hat{\boldsymbol{A}}_i \otimes \hat{\boldsymbol{B}}_i \otimes \hat{\boldsymbol{C}}_{i_j}]^\dagger vec(\mathcal{F}_l)$. The obtained core tensors $\tilde{\mathcal{H}}_{ij}$ are used as monitoring features under the assumption that they follow a tensor normal distribution $\tilde{\mathcal{H}}_{ij}^{(l)} \sim N(\bar{\mathcal{H}}_{ij}^{(l)}, \hat{\boldsymbol{\Sigma}}_1^{(l)}, \hat{\boldsymbol{\Sigma}}_2^{(l)}, \hat{\boldsymbol{\Sigma}}_3^{(l)})$ or equivalently $vec(\tilde{\mathcal{H}}_{ij}^{(l)}) \sim N(vec(\bar{\mathcal{H}}_{ij}^{(l)}), \hat{\boldsymbol{\Sigma}}_3^{(l)} \otimes \hat{\boldsymbol{\Sigma}}_2^{(l)} \otimes \hat{\boldsymbol{\Sigma}}_1^{(l)})$, where $\bar{\mathcal{H}}_{ij}^{(l)}$ is the core tensor mean, and $\hat{\boldsymbol{\Sigma}}_i^{(l)}$ is the covariance matrix along mode i.

3) Between-sample Monitoring: In AM process, each sample can be regarded as the stacking of multiple layers that are

collection of a sequence of frames. Between-sample monitoring strategy monitors the printing process at the sample level. We denote an input sample as $\mathcal{U} \in \mathbb{R}^{I_1 \times I_2 \times I_3 \times I_4}$. The first and second dimensions, I_1 and I_2, correspond to the width and height of a single image frame, respectively. The third dimension I_3 corresponds to the number of frames recorded for printing one layer, and the fourth dimension I_4 corresponds to the number of layers. Then, given N in-control samples $\mathcal{U}_k \in \mathbb{R}^{I_1 \times I_2 \times I_3 \times I_4}$; $k = 1, 2, \cdots, N$, the basis matrices and the core tensor are extracted using the following optimization:

$$\hat{\mathcal{Q}}^{(k)}, \hat{\boldsymbol{A}}, \hat{\boldsymbol{B}}, \hat{\boldsymbol{C}}, \hat{\boldsymbol{D}} = \underset{\mathcal{Q}^{(k)}, \boldsymbol{A}, \boldsymbol{B}, \boldsymbol{C}, \boldsymbol{D}}{\operatorname{argmin}} \sum_{k=1}^{N} \|\mathcal{U}_k - \sum_{p=1}^{R_1}\sum_{q=1}^{R_2}\sum_{r=1}^{R_3}\sum_{l=1}^{R_4} q_{pqrl}^{(k)} \boldsymbol{a}_p \circ \boldsymbol{b}_q \circ \boldsymbol{c}_r \circ \boldsymbol{d}_l\|_F^2$$

$$= \underset{\mathcal{Q}^{(k)}, \boldsymbol{A}, \boldsymbol{B}, \boldsymbol{C}, \boldsymbol{D}}{\operatorname{argmin}} \sum_{k=1}^{N} \|\mathcal{U}_k - [\![\mathcal{Q}^{(k)}; \boldsymbol{A}, \boldsymbol{B}, \boldsymbol{C}, \boldsymbol{D}]\!]\|_F^2 \quad (8)$$

Subject to $\mathcal{Q}^{(k)} \in \mathbb{R}^{R_1 \times R_2 \times R_3 \times R_4}$, $\boldsymbol{A} \in \mathbb{R}^{I_1 \times R_1}$, $\boldsymbol{B} \in \mathbb{R}^{I_2 \times R_2}$, $\boldsymbol{C} \in \mathbb{R}^{I_3 \times R_3}$,$\boldsymbol{D} \in \mathbb{R}^{I_4 \times R_4}$ and column-wise orthogonality for $\boldsymbol{A}, \boldsymbol{B}, \boldsymbol{C}, \boldsymbol{D}$ where $\boldsymbol{A}, \boldsymbol{B}, \boldsymbol{C}, \boldsymbol{D}$ are the basis matrices corresponding to the first, second, third and fourth dimension of input sample $\mathcal{U}$, respectively. $\hat{\mathcal{Q}}^{(k)}$ is the extracted core tensor for the k_{th} sample $\mathcal{U}_k$; $k = 1, 2, \cdots, N$, and $q_{pqrl}^{(k)}$ is the $(p, q, r, l)_{th}$ element of $\mathcal{Q}^{(k)}$.

Let $\mathcal{V} \in \mathbb{R}^{I_1 \times I_2 \times I_3 \times I_4 \times N}$ denote the tensor of N in-control samples $\mathcal{U}_k$; $k = 1, 2, \cdots, N$. Using proposition 1, we can argue that the basis matrices $\hat{\boldsymbol{A}}$, $\hat{\boldsymbol{B}}$, $\hat{\boldsymbol{C}}$ and $\hat{\boldsymbol{D}}$ obtained through Tucker decomposition of $\mathcal{V}$ provide the same solutions to (8)

$$\hat{\mathcal{T}}, \hat{\boldsymbol{A}}, \hat{\boldsymbol{B}}, \hat{\boldsymbol{C}}, \hat{\boldsymbol{D}}, \hat{\boldsymbol{E}} = \underset{\mathcal{T}, \boldsymbol{A}, \boldsymbol{B}, \boldsymbol{C}, \boldsymbol{D}, \boldsymbol{E}}{\operatorname{argmin}} \|\mathcal{V} - \sum_{p=1}^{R_1}\sum_{q=1}^{R_2}\sum_{r=1}^{R_3}\sum_{l=1}^{R_4}\sum_{h=1}^{R_5} t_{pqrlh} \boldsymbol{a}_p \circ \boldsymbol{b}_q \circ \boldsymbol{c}_r \circ \boldsymbol{d}_l \circ \boldsymbol{e}_h\|_F^2$$

$$= \underset{\mathcal{T}_i, \boldsymbol{A}_i, \boldsymbol{B}, \boldsymbol{C}, \boldsymbol{D}, \boldsymbol{E}}{\operatorname{argmin}} \|\mathcal{V} - [\![\mathcal{T}; \boldsymbol{A}, \boldsymbol{B}, \boldsymbol{C}, \boldsymbol{D}, \boldsymbol{E}]\!]\|_F^2 \quad (9)$$

Subject to $\mathcal{T} \in \mathbb{R}^{R_1 \times R_2 \times R_3 \times R_4 \times R_5}$, $\boldsymbol{A} \in \mathbb{R}^{I_1 \times R_1}$, $\boldsymbol{B} \in \mathbb{R}^{I_2 \times R_2}$, $\boldsymbol{C} \in \mathbb{R}^{I_3 \times R_3}$, $\boldsymbol{D} \in \mathbb{R}^{I_4 \times R_4}$, $\boldsymbol{E} \in \mathbb{R}^{N \times R_5}$ and columnwise orthogonality for $\boldsymbol{A}, \boldsymbol{B}, \boldsymbol{C}, \boldsymbol{D}, \boldsymbol{E}$ where $\boldsymbol{E}$ is the basis matrix corresponding to the last dimension (sample) of tensor $\mathcal{V}$, $\hat{\mathcal{T}}$ is the extracted core tensor and t_{pqrlh} is the $(p, q, r, l, h)_{th}$ element of core tensor $\mathcal{T}$. Using proposition 1, given $\hat{\mathcal{T}}$ and $\hat{\boldsymbol{E}}$ the core tensor $\hat{\mathcal{Q}}^{(k)}$ in (8) can be obtained by:

$$\hat{q}_{pqrl}^{(k)} = \sum_{h=1}^{R_5} \hat{e}_h^{(k)} \times \hat{t}_{pqrlh} \quad (10)$$

where $\hat{e}_h^{(k)}$ is the $(k, h)_{th}$ element of matrix $\hat{\boldsymbol{E}}$. These N core tensors are used as features to setup the control chart for between-sample monitoring and estimate the necessary parameters. For online monitoring, using the learnt basis matrices $\hat{\boldsymbol{A}}, \hat{\boldsymbol{B}}, \hat{\boldsymbol{C}}, \hat{\boldsymbol{D}}$, we then determine the core tensor feature $\mathcal{Q}^{(w)}$ for a new sample $\mathcal{U}_w$, using the following optimization:

$$\tilde{\mathcal{Q}}^{(w)} = \underset{\mathcal{Q}^{(w)}}{\operatorname{argmin}} \|\mathcal{U}_w - \sum_{p=1}^{R_1}\sum_{q=1}^{R_2}\sum_{r=1}^{R_3}\sum_{l=1}^{R_4} q_{pqrl}^{(w)} \hat{\boldsymbol{a}}_p \circ \hat{\boldsymbol{b}}_q \circ \hat{\boldsymbol{c}}_r \circ \hat{\boldsymbol{d}}_l\|_F^2$$

$$= \underset{\mathcal{Q}^{(w)}}{\operatorname{argmin}} \|\mathcal{U}_w - [\![\mathcal{Q}^{(w)}; \hat{\boldsymbol{A}}, \hat{\boldsymbol{B}}, \hat{\boldsymbol{C}}, \hat{\boldsymbol{D}}]\!]\|_F^2 \quad (11)$$

To increase the computation efficiency, we can rewrite the above objective function in vectorized form as $\|vec(\mathcal{U}_w) - (\hat{\boldsymbol{A}} \otimes \hat{\boldsymbol{B}} \otimes \hat{\boldsymbol{C}} \otimes \hat{\boldsymbol{D}}) vec(\mathcal{Q}^{(w)})\|^2$, with the closed-form solution in the form of $vec(\tilde{\mathcal{Q}}_w) = (\hat{\boldsymbol{A}} \otimes \hat{\boldsymbol{B}} \otimes \hat{\boldsymbol{C}} \otimes \hat{\boldsymbol{D}})^T vec(\mathcal{U}_w)$. Therefore, the core tensor for an incoming sample becomes $\tilde{\mathcal{Q}}^{(w)} = \mathcal{U}_w \times_1 \hat{\boldsymbol{A}}^T \times_2 \hat{\boldsymbol{B}}^T \times_3 \hat{\boldsymbol{C}}^T \times_4 \hat{\boldsymbol{D}}^T$. To monitor the core tensor $\tilde{\mathcal{Q}}^{(w)}$, we assume that they follow tensor normal distribution $\tilde{\mathcal{Q}}^{(w)} \sim N(\bar{\mathcal{Q}}^{(w)}, \hat{\boldsymbol{\Sigma}}_1^{(w)}, \hat{\boldsymbol{\Sigma}}_2^{(w)}, \hat{\boldsymbol{\Sigma}}_3^{(w)}, \hat{\boldsymbol{\Sigma}}_4^{(w)})$ or equivalently $vec(\tilde{\mathcal{Q}}^{(w)}) \sim N(vec(\bar{\mathcal{Q}}^{(w)}), \hat{\boldsymbol{\Sigma}}_4^{(w)} \otimes \hat{\boldsymbol{\Sigma}}_3^{(w)} \otimes \hat{\boldsymbol{\Sigma}}_2^{(w)} \otimes \hat{\boldsymbol{\Sigma}}_1^{(w)})$ where $\bar{\mathcal{Q}}^{(w)}$ is the core tensor mean, and $\hat{\boldsymbol{\Sigma}}_i^{(w)}$ is the covariance matrix along mode i.

B. Monitoring Statistics

Based on the multivariate normal assumption on the extracted features (i.e., the core tensors at the frame, layer and sample levels), we propose to use Hotelling's T-squared control chart for monitoring the process. We denote the p-dimensional extracted features as $\boldsymbol{\theta_w}$ for the new sample, which is the vectorized form of the core tensor. The T^2 monitoring statistics is calculated as $N(\boldsymbol{\theta_w} - \bar{\boldsymbol{\theta}})\boldsymbol{S}^{-1}(\boldsymbol{\theta_w} - \bar{\boldsymbol{\theta}})$, where $\bar{\boldsymbol{\theta}}$ and $\boldsymbol{S}$ are the mean and covariance learnt from the N in-control samples. For example, the $\bar{\boldsymbol{\theta}}$ and $\boldsymbol{S}$ for the between-layer monitoring features are $vec(\bar{\mathcal{G}}_i)$ and $(\hat{\boldsymbol{\Sigma}}_3 \otimes \hat{\boldsymbol{\Sigma}}_2 \otimes \hat{\boldsymbol{\Sigma}}_1)$, respectively. $\bar{\boldsymbol{\theta}}$ is calculated as $\frac{\sum_{k=1}^{N} \boldsymbol{\theta}_k}{N}$ where $\boldsymbol{\theta}_k$; $k = 1, 2, \cdots, N$ is the extracted feature vector for the core tensor of the k_{th} in-control sample. The covariance $\boldsymbol{S}$ is calculated as $\sum_{k=1}^{N} \frac{1}{N-1}(\boldsymbol{\theta}_k - \bar{\boldsymbol{\theta}})(\boldsymbol{\theta}_k - \bar{\boldsymbol{\theta}})^T$.

The transformed T^2 statistics $\frac{N-p}{(N-1)p} N(\boldsymbol{\theta_w} - \bar{\boldsymbol{\theta}})\boldsymbol{S}^{-1}(\boldsymbol{\theta_w} - \bar{\boldsymbol{\theta}})$ follows an F-distribution with p and $N - p$ degrees of freedom [26]. The $(1-\alpha)100$ percentile of the F-distribution can be used to determine the control limits. However, in the cases where the normality assumption may not be valid, empirical distributions of the core tensors obtained from the training data set are used to determine the control limits. The number of features is determined by the length of the vectorized core tensors. The dimension of the core tensors is determined based on the Bayesian Information Criterion (BIC) using [27]:

$$\underset{\hat{\mathcal{G}}}{\operatorname{argmax}}\, BIC(\hat{\mathcal{G}}) = 2M \ln(\|\mathcal{G} - \hat{\mathcal{G}}\|_F) + L \ln(M) + C \quad (12)$$

where original tensor $\mathcal{G}$ has M elements, L is the number of free parameters in $\hat{\mathcal{G}}$ and C is a constant independent of $\hat{\mathcal{G}}$.

IV. Simulation Study

The simulation study presented in this section relies on real video image data acquired during the L-PBF process of stainless steel specimens. This data set were then processed to simulate realistic process anomalies at different levels and with different severity. An L-PBF prototype system, called Penelope, characterized by an open and highly sensorized architecture was used. The system is quipped with a IPG YLR-150/750-QCW-AC single mode fiber, a Ytterbium-doped yttrium aluminum garnet (Yb:YAG) laser source (maximum power of 250 W and a wavelength of 1060 nm). The industrial scan head ScanLab Hurryscan14 is controlled by an Optoprim EC1000 controller, while the prototype control is based on an

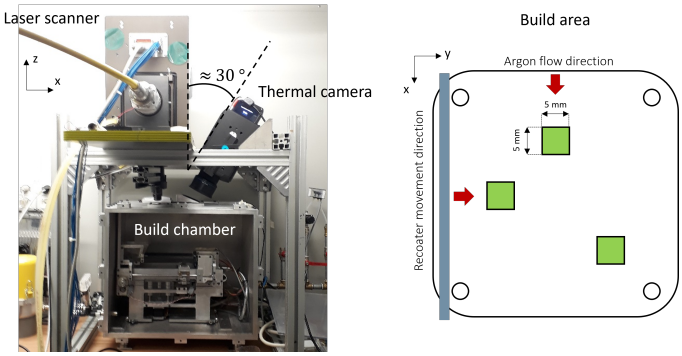

Fig. 4. Experimental setup (left) and the placement of the specimens produced with nominal process parameters within the build area (right).

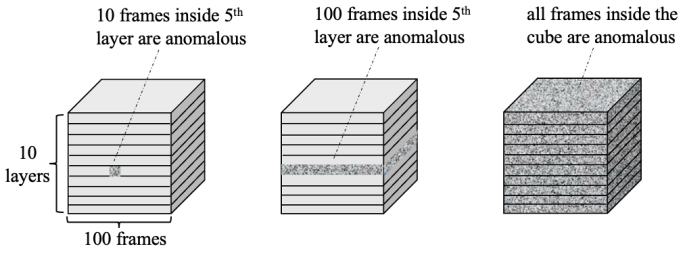

Fig. 5. The local anomaly starts in the middle of 5_{th} layer and lasts for 10 frames (left), the layer-wise anomaly occurs at the 5_{th} layer (middle) and the sample-wise anomaly (right).

in-house produced controller. The build chamber operates in an inert environment, filled with argon. Additional details about the L-PBF system can be found in [28]. The experimentation involved the production of cubic specimens of size 5 x 5 x 5 mm with gas-atomized AISI 316L powder with average particle size of 25 μm. The cubes were printed with different energy density levels by varying the laser power. For the simulation case study presented in this section, only three cubes printed with the nominal laser power of 225W were considered. All other process parameters were set at nominal values: layer thickness t=50 μm, scan speed v=500 mm/s and hatch spacing h=70 μm. During the L-PBF, infrared videos were acquired by means of a FLIR X6580sc thermal camera, operating in the spectral range 3 - 5 μ m, calibrated in a temperature range of $300 - 1500°C$. The videos were acquired with a frame rate of 100 fps and a spatial resolution of about 200 μm/pixel. Figure 4 shows the experimental setup and the placement of the specimens produced with nominal process parameters within the build area. The infrared videos acquired in 10 non-consecutive layers were then post-processed to introduce realistic variations of local and global heating and cooling patters, representative of different types of process anomalies. Three different types of anomalies were selected and simulated. The first set consists of a hot-spot event, i.e., a region of the layer that stays hot for a long time after the laser beam displaces to a different region. This anomaly has been discussed in previous studies [29][16], and it is known to be a possible driver of micro and macro geometrical distortions and/or micro-structural discontinuities. It is therefore representative of a local anomaly affecting a small location of a single layer (the anomaly may disappear in following layers to the variation of the scan strategy). Hot-spots of different sizes were introduced and simulated following the same approach presented in [16], by modifying the time history of pixel intensities within a given area. The second anomaly consists of a global change of the thermal history of the process in one whole layer, which may disappear in following layers. An over-heating effect was simulated by multiplying the intensity of every pixel by a so-called temperature increase factor, starting from the frame where the pixel was heated up to the melting temperature by the laser. This anomaly is representative of a global over-heating effect occurring in one layer as a consequence of either a change of the inter-layer cooling time or a diminished heat flux towards the surroundings (e.g., in large overhang areas). This anomaly may lead to micro-structural discontinuities and porosity in the part. The third anomaly consists of a global under-heating effect involving a large portion of the layer and persisting through all consecutive layers, possibly affecting the whole part. It can be representative of a laser beam attenuation, induced by a dirty laser window, i.e., by an excessive deposition of vaporized metal on the window through which the laser beam is headed to the material. A decrease of the energy input may cause so-called lack-of-fusion defects, i.e., pores and discontinuities resulting from a non complete melting and solidification of the layer. In this case, the pixel intensities within a given area in multiple layers were multiplied by a temperature decrease factor to simulate the anomaly.

These three anomalies were selected as they are representative of real process anomalies in L-PBF that may occur at either local, layer-wise and sample-wise level, respectively (see Figure 5). Figure 6 shows, in false color (revealing or enhancing features otherwise invisible or poorly visible to a human eye), an example of video frames from an in-control IR video recording during the production of one part and examples of video frames from simulated anomalies. In Figure 6, the video frame area roughly coincides with the area scanned by the laser during the production of our specimen. The peak temperature is achieved in the melt pool, were the laser melts the powder, and a heat affected zone is present as well, characterized by a quickly decreasing temperature as the laser moves along the predefined path melting other regions of the layer.

The simulation study was designed to evaluate the performance of the within-layer, between-layer and between-sample monitoring approach, separately. The video image data recorded during the production of one specimen in one layer can be considered as a tensor sample of size $32 \times 26 \times 100 \times 10$, where 32x26 is the size in pixels of the region of interest corresponding to the area scanned by the laser to produce one layer of the specimen, 10 is the number of monitored layers and 100 is the number of frames in the infrared video of L-PBF of one specimen, in one layer.

The simulation can be split into two phases. In the first phase, 100 normal (in-control) samples were generated based on a single recorded video of the nominal L-PBF process.

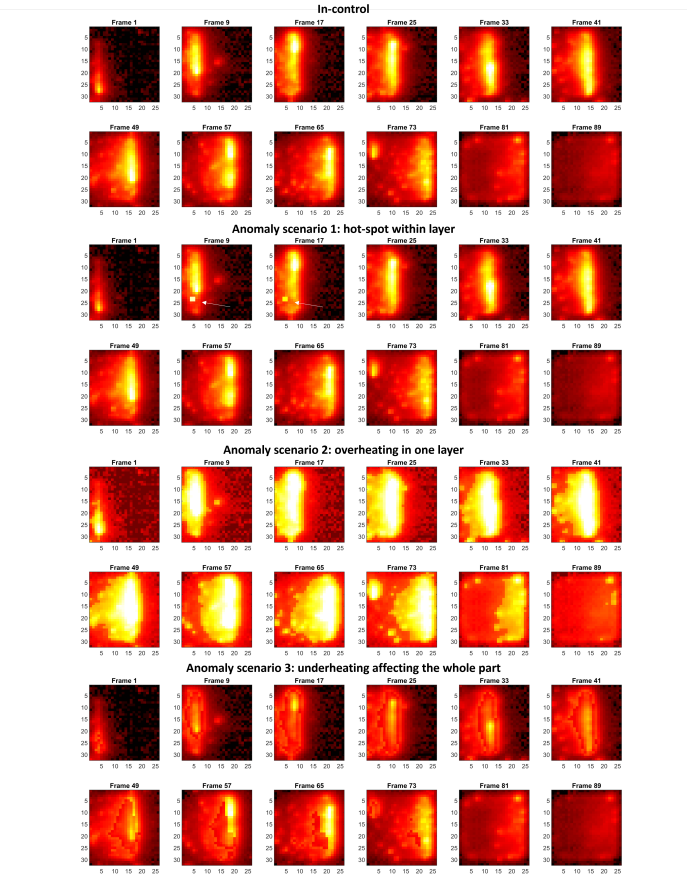

Fig. 6. Example of video frames from an in-control IR video recording during the production of one part and examples of video frames from simulated anomalies.

To simulate 100 replicates of the same in-control L-PBF, we added a Gaussian noise to the pixel intensity of each frame. To be specific, the noise added to the pixel at the i_{th} row and the j_{th} column of a frame follows a normal distribution $N(0, \sigma_{ij})$ where the σ_{ij} equals to the product of a prespecified noise factor and the average magnitude of the pixels (i, j) across all frames at the current layer. Intuitively speaking, the noise factor is acting like a signal-to-noise ratio. Hence, a large variance of the noise is expected for a pixel with a large average intensity. For each replication of the process, we extracted the features using the proposed methods, which are then used to calculate T^2 monitoring statistics and build the control charts. The control limit was chosen so that the false alarm rate in the first phase of the analysis for each of the three monitoring methods was 1% under different anomalous scenarios. We generated another 100 in-control samples and further confirmed that selected the control limit results in a false alarm rate around predetermined 1% for the three monitoring methods. This was followed by another 100 out-of-control samples generated by inserting the aforementioned anomalies. To compare the performance of the three proposed methods, the miss detection rate was used as the performance criteria. As these monitoring methods monitor the process at different resolutions, we define a sample-wise miss detection so that the results obtained for different monitoring methods are comparable.

TABLE I
THE SAMPLE-WISE MISS DETECTION OF THE HIERARCHICAL PROCESS MONITORING METHOD UNDER THREE ANOMALOUS SCENARIOS AND THREE LEVELS OF NOISE FACTORS

		Low noise	Medium noise	High noise
Hot-spot anomaly	size = 1	0	0.20	0.97
	size = 2	0	0	0
	size = 3	0	0	0
Overheating anomaly	offset = 5	0	0	0.03
	offset = 10	0	0	0
	offset = 15	0	0	0
Dirty window anomaly	decrease factor = 0.98	0	0	0.03
	decrease factor = 0.96	0	0	0
	decrease factor = 0.94	0	0	0

To assess the sensitivity of the different monitoring methods, three different noise factors corresponding to three levels of noise were considered for each type of anomaly. To quantify the performance of the different monitoring methods, we determined their miss detection rates for each anomalous scenario in the phase II analysis. The sample-wise miss detection rate was calculated as the fraction of out-of-control samples which were labeled as in-control samples by the monitoring methods.

Before demonstrating the individual performance of the three different monitoring methods, we presented in Table I the performance of the hierarchical process monitoring approach as a whole as described in Figure 2. Table 1 shows that the hierarchical monitoring approach is very effective in detecting all types of anomalies, with miss detection errors observed only when the severity of the anomaly was very low and the image noise quite high. Indeed, under these conditions, the noise may mask the occurrence of the anomaly, especially when it is a local one.

In Figure 7, we compared the performance of the three monitoring approaches in terms of sample-wise miss detection rate for the hot-spot anomaly with three different sizes (i.e. three different hot-spot severity) under three levels of noise. In all cases, the within-layer monitoring strategy showed the lowest miss detection rate. This confirms that a monitoring tool designed to detect anomalies on the frame scale outperforms monitoring tools designed to detect anomalies on layer or sample scales.

In Figure 8, we compared the performance of the three monitoring strategies in terms of sample-wise miss detection rate for the global overheating anomaly with three different temperature offsets (i.e., three different severity levels), under three levels of noise. For this type of anomaly, as expected, the between-layer monitoring strategy had the lowest miss detection rate in all cases while the within-layer monitoring strategy led to the highest miss detection rate. This confirms that a monitoring tool designed to detect anomalies on the

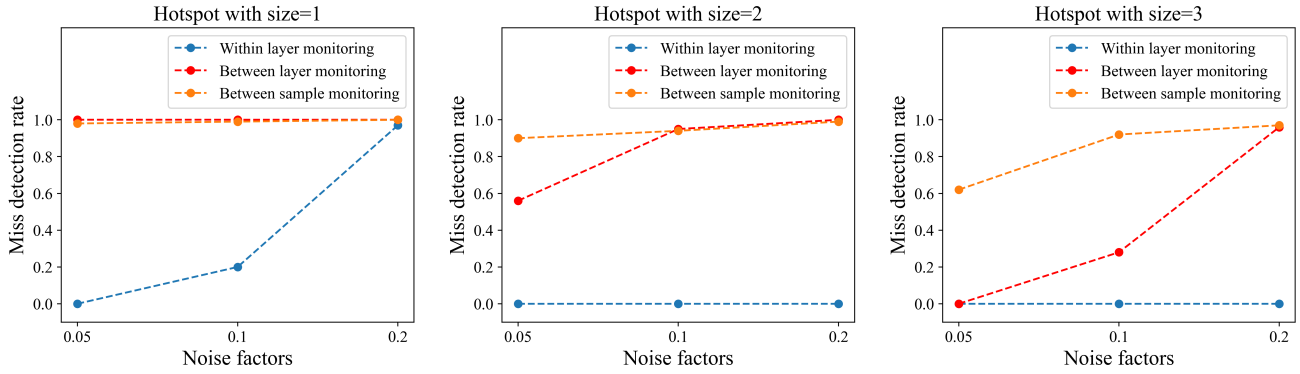

Fig. 7. The sample-wise miss detection rate for the hot-spot anomaly with three different sizes under three levels of noise factors

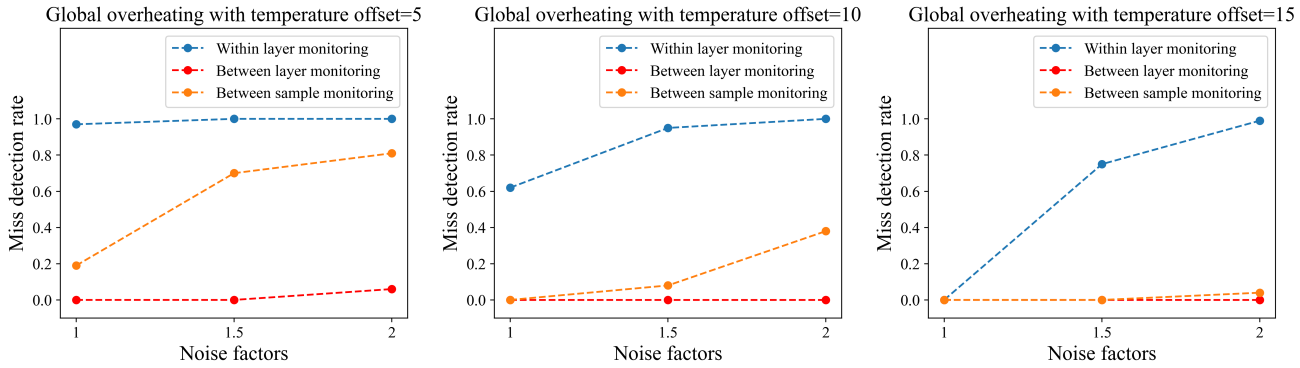

Fig. 8. The sample-wise miss detection rate for the global overheating anomaly with three temperature offsets under three levels of noise factors

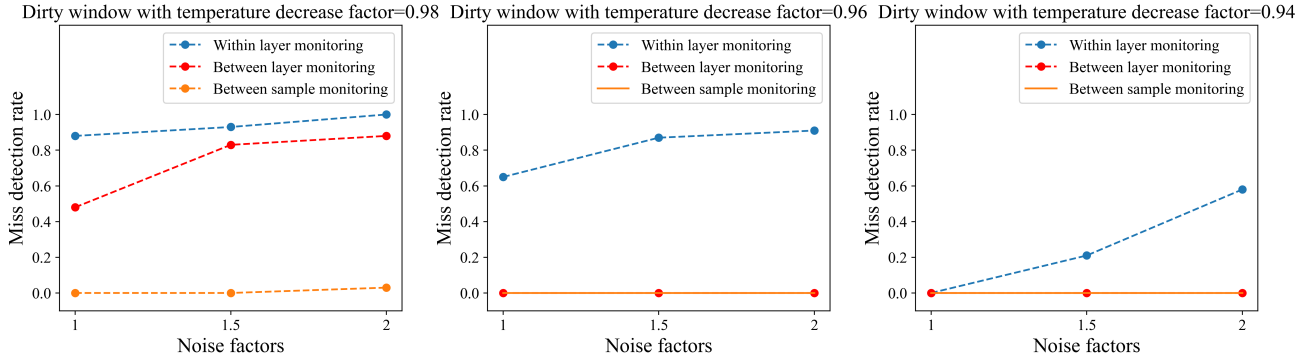

Fig. 9. The sample-wise miss detection rate for the dirty window anomaly with three temperature decrease factors under three levels of noise factors

layer scale outperforms monitoring tools designed to detect anomalies on frame or sample levels.

In Figure 9, we compared the performance of the three-level monitoring strategies in terms of sample-wise miss detection rate for the third anomaly type involving a global energy attenuation simulating the effect of a dirty laser window with three different temperature decrease factors under three levels of noise. For this type of anomaly, the between-sample monitoring strategy had the lowest miss detection rate at the lowest severity level while having the same miss detection rate as the between-layer monitoring strategies at the two highest severity levels. The performance of the within-layer monitoring was the worst in all cases for this anomaly type. This confirms that a monitoring tool designed to detect anomalies on a global scale outperforms monitoring tools designed to detect anomalies on the frame or layer scale. Generally speaking, an increasing noise level in the input data yielded a decreased monitoring performance for all the three monitoring methods.

As mentioned before, the miss detection rates of the within-layer and between-layer monitoring methods were converted to sample-wise to be consistent with the sample-wise miss detection rate associated with between-sample monitoring method for the comparison purpose. However, in order to reveal the real performance of within-layer and between-layer monitoring methods at their own scales, we also determined the frame-wise miss detection rate of the within-layer moni-

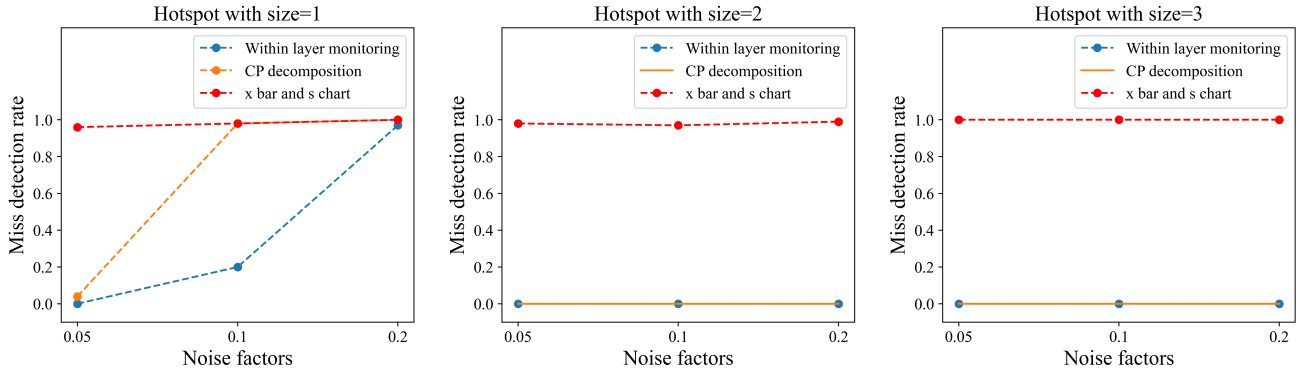

Fig. 10. The sample-wise miss detection rate for the hot-spot anomaly with three different sizes under three levels of noise factors

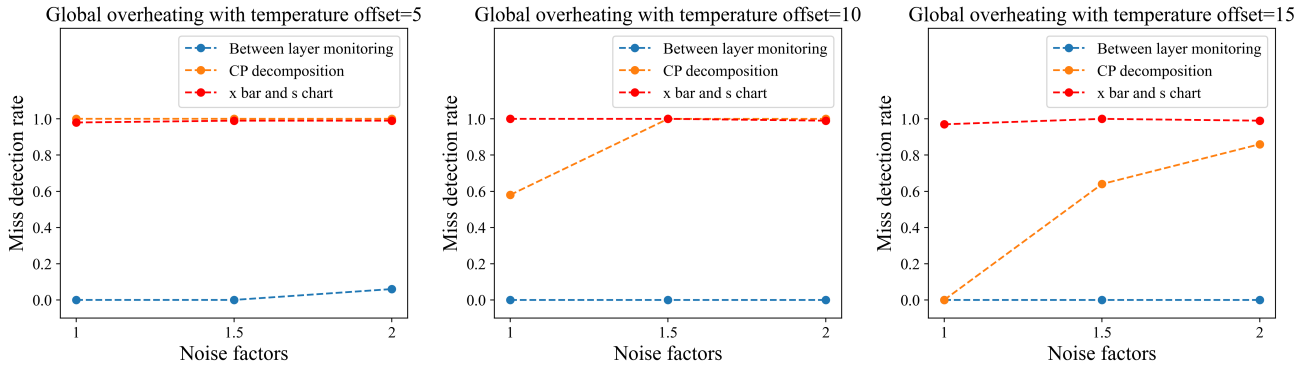

Fig. 11. The sample-wise miss detection rate for the global overheating anomaly with three temperature offsets under three levels of noise factors

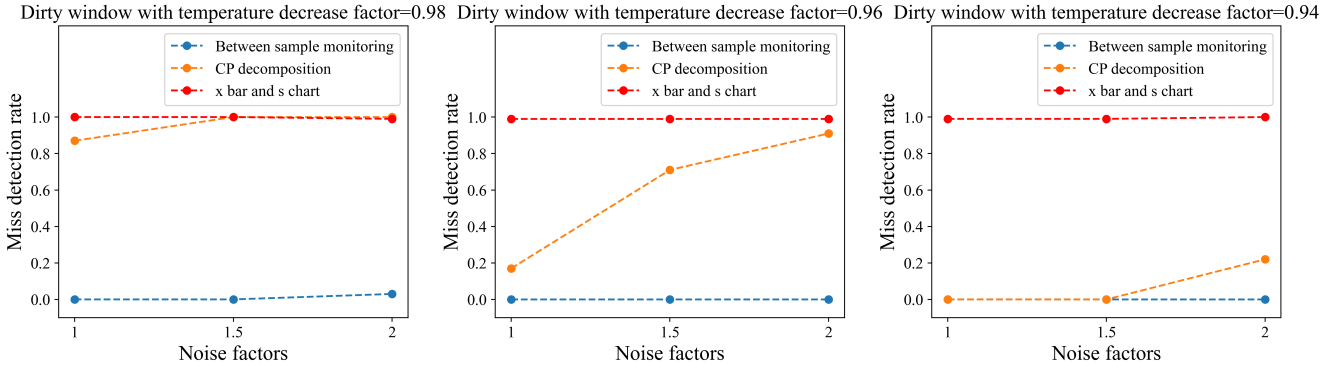

Fig. 12. The sample-wise miss detection rate for the underheating anomaly affecting the whole part with three temperature decrease factors under three levels of noise factors

toring method, and the layer-wise miss detection rate of the between-layer monitoring method for the three anomalous scenarios. The results summarized in Appendix D, confirm the need to combine process monitoring capabilities at different levels to achieve high anomaly detection performances in the presence of out-of-control states that may occur on different scales.

To further evaluate our proposed monitoring strategies, we also compare its performance against other benchmarks. The first benchmark we considered in our study is a monitoring method that uses tensor rank-one decomposition or equivalently CP decomposition for within-layer monitoring proposed by Yan et al [20]. We selected this benchmark since CP demonstrates better performance compared with other feature extraction methods such as unfold principal analysis (UPCA) and uncorrelated multilinear principal component analysis (UMPCA) as mentioned in a study by Yan et al [20]. The other benchmark is the joint Shewhart X-bar and s control charts. This traditional control charting approach was selected as it is the most common approach practitioners may adopt, as it basically translates the information content of the video data into simple synthetic statistics. The subgroup size in our study is the number of pixels in an image frame. It is worth noting that both X-bar and s charts, and CP decomposition

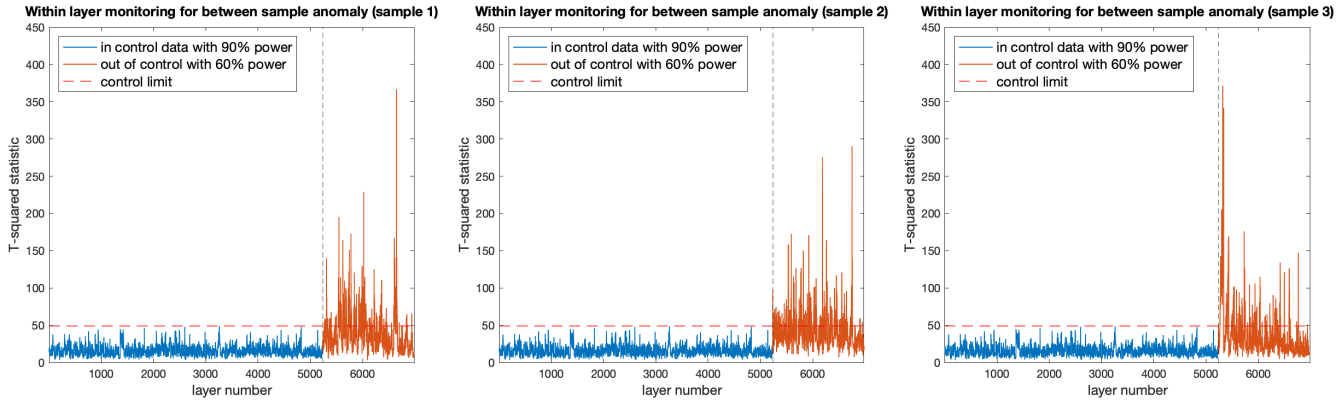

Fig. 13. The control charts of within-layer monitoring for between-sample anomaly: test sample one (left); test sample two (middle); test sample three (right)

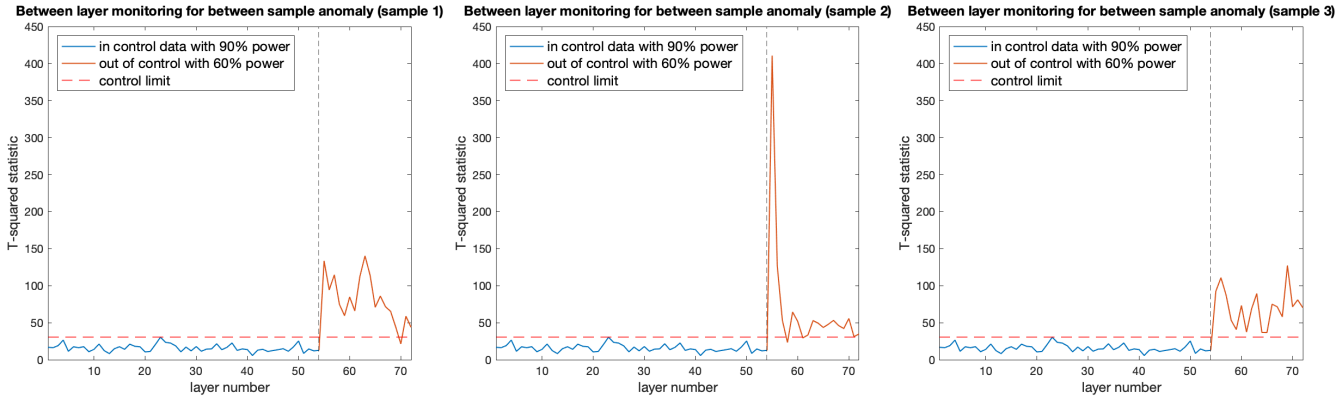

Fig. 14. The control charts of between-layer monitoring for between-sample anomaly: test sample one (left); test sample two (middle); test sample three (right)

were implemented as within-layer monitoring approach, due to the lack of a hierarchical monitoring scheme.

In Figure 10, 11 and 12, we show the miss detection rate for our proposed monitoring method as well as the other two benchmarks in the presence of the three simulated anomalies. In all the cases, the performance of the X-bar and s charts is the worst. Its poor performance is attributed to the loss of spatial information at each frame level. Also, the performance of CP decomposition is considerably worse than that of our proposed monitoring strategies in most cases even though the performance gap between CP decomposition and our proposed monitoring approach decreases as the severity level of the anomaly increases. The CP decomposition can be viewed as a special case of Tucker decomposition where core tensor is superdiagonal and each dimension of the core tensor is the same. Therefore, the Tucker decomposition offers much more flexibility. This can also contribute to the better performance of our method in addition to its hierarchical advantage.

V. Case Study

In this section, we show the application of the proposed methodology in a case study where a sample-wise change was induced by producing copies of the same cubic specimens by varying the laser power rather than using simulations. The same prototype experimentation and L-PBF setup described in the previous section was adopted. During the process, the infrared videos were acquired for 18 non-consecutive layers. Two sets of AISI 316L cubic specimens were produced in the same build: three specimens produced with a nominal laser power of 225 W (90% of the maximum laser power), and three specimens produced with a decreased laser power of 150 W (60% of the maximum laser power). Hence, the dataset consists of three replicates of the process in its natural (in-control) conditions, and three replicates in an out-of-control condition, where the decreased laser power caused a severe lack-of-fusion porosity. This type of out-of-control condition is representative of a sample-wise anomaly. However, the small number of specimens did not allow the design and test of the sample-wise monitoring level. The hierarchical approach was therefore applied and tested in a version that consists of two levels only, i.e., the within-layer and between-layer levels. The results of the proposed approach in this real case study are shown in Figure 13 and Figure 14, showing the control charts associated to the within-layer and between-layer monitoring levels, respectively. Figure 13 and Figure 14 show that both the monitoring levels allow detecting the change in the processing conditions. The between-layer monitoring tool is able to detect the change at the first layer of the sample affected by the change, for all the monitored specimens. The within-layer monitoring tool is able to quickly detect the

change as well. As far as the out-of-control sample 1 is concerned, the anomaly is detected after 32 frames, during the production of the first anomalous layer, whereas for the other two samples, the anomaly was signalled since the first video-frame during the production of the first anomalous layer. According to our framework shown in the Figure 2, the fact that the anomaly is detected by both the within-layer and between-layer monitoring control charts suggests that a global anomaly is present, which affects the entire layer and is sustained for all successive layers. It is also worth noting that, in this case study, the within-layer and between-layer monitoring methods signal in the presence of a global anomaly because of the high severity of the anomaly itself. However, as shown in the previous section, for sample-level anomalies with a lower severity these two methods may not be effective in detecting the change.

VI. Conclusion

In a variety of manufacturing processes, out-of-control shifts may occur at different levels and on different scales. AM processes represent one example of applications, where anomalies may range from local to global ones, causing changes within the single layer, from one layer to another or from one part to another. Other example can be found in manufacturing processes that can be decomposed into different stages and/or different observation scales, e.g., in batch processes where anomalies may affect the process behaviour within the batch, its variability from batch to batch or from part to part. The proposed hierarchical monitoring tackled the lack of process monitoring techniques suitable to deal with multi-level/multi-scale anomalies. It is capable of detecting a wide range of anomalies, and at the same time, enhancing the flexibility of process monitoring while preserving its performances in terms of false positives and miss detection rates. The numerical studies described in this study showed the potential of this approach for in-line and in-situ anomaly detection in AM, where the relevant information content in thermal video-image streams is effectively extracted and analyzed through a tensor based decomposition scheme. The simulation analysis showed the potential of the method to detect process shifts occurring on different spatial and temporal scales and with different severity, also highlighted its better performance compared to the benchmark methods that lack the multi-resolution capability.

Future research will be devoted to further test and validate the proposed approach for different types of real anomalies, together with the possible extension and adaptation of the method to other manufacturing processes and applications. We also plan to extend our work from fault detection to fault diagnosis in future studies. Although our proposed monitoring method offers information about the scale of the anomalies, one complementary aim is to pinpoint the nature of the detected anomaly, supporting the diagnostic analysis.

Appendix A

Firstly, we show $\|\mathcal{Y}\|_F^2 = \sum_{i=1}^N \|\mathcal{X}_i\|_F^2$. By vectorizing tensor $\mathcal{X}_i$ for $i = 1, 2, \cdots, N$, $vec(\mathcal{Y})$ can be written as $[vec(\mathcal{X}_1), vec(\mathcal{X}_2), \cdots, vec(\mathcal{X}_N)]^T$. It is easy to see that $\|\mathcal{Y}\|_F^2 = \sum_{i=1}^N \|\mathcal{X}_i\|_F^2$. Next, we show the basis matrix obtained through (2) is the same solution as obtained through (1). Using the fact $\|\mathcal{Y}\|_F^2 = \sum_{i=1}^N \|\mathcal{X}_i\|_F^2$

$$\underset{\mathcal{S}_i, \boldsymbol{A_i}, \boldsymbol{B_i}, \boldsymbol{C_i}, \boldsymbol{D_i}}{\operatorname{argmin}} \|\mathcal{Y} - \sum_{p=1}^{R_1}\sum_{q=1}^{R_2}\sum_{r=1}^{R_3}\sum_{l=1}^{R_4} s_{i_{pqrl}} \boldsymbol{a}_{i_p} \circ \boldsymbol{b}_{i_q} \circ \boldsymbol{c}_{i_r} \circ \boldsymbol{d}_{i_l}\|_F^2$$

$$= \underset{\mathcal{S}_i, \boldsymbol{A_i}, \boldsymbol{B_i}, \boldsymbol{C_i}}{\operatorname{argmin}} \sum_{k=1}^{N} \|\mathcal{X}_k - \sum_{p=1}^{R_1}\sum_{q=1}^{R_2}\sum_{r=1}^{R_3}(\sum_{l=1}^{R_4} d_{i_l}^{(k)} * s_{i_{pqrl}}) \boldsymbol{a}_{i_p} \circ \boldsymbol{b}_{i_q} \circ \boldsymbol{c}_{i_r}\|_F^2$$

By comparing this with (1), we can see that $\boldsymbol{A_i}, \boldsymbol{B_i}, \boldsymbol{C_i}$ obtained using above optimization is also the solution to (1) and $\sum_{l=1}^{R_4} d_{i_l}^{(k)} \times s_{i_{pqrl}} = g_{i_{pqr}}^{(k)}$.

Appendix B

Through rewriting the objective function (3) in a vectorized form as $\|vec(\mathcal{X}_m) - (\hat{\boldsymbol{A}}_i \otimes \hat{\boldsymbol{B}}_i \otimes \hat{\boldsymbol{C}}_i) vec(\mathcal{G}_i^{(m)})\|^2$, the closed form solution can be obtained by $vec(\mathcal{G}_i^{(m)}) = ((\hat{\boldsymbol{A}}_i \otimes \hat{\boldsymbol{B}}_i \otimes \hat{\boldsymbol{C}}_i)^T (\hat{\boldsymbol{A}}_i \otimes \hat{\boldsymbol{B}}_i \otimes \hat{\boldsymbol{C}}_i))^{-1} (\hat{\boldsymbol{A}}_i \otimes \hat{\boldsymbol{B}}_i \otimes \hat{\boldsymbol{C}}_i)^T vec(\mathcal{X}_m) = ((\hat{\boldsymbol{A}}_i^T \otimes \hat{\boldsymbol{A}}_i)(\hat{\boldsymbol{B}}_i^T \otimes \hat{\boldsymbol{B}}_i)(\hat{\boldsymbol{C}}_i^T \otimes \hat{\boldsymbol{C}}_i))^{-1} (\hat{\boldsymbol{A}}_i \otimes \hat{\boldsymbol{B}}_i \otimes \hat{\boldsymbol{C}}_i)^T vec(\mathcal{G}_i^{(m)}) = (\hat{\boldsymbol{A}}_i \otimes \hat{\boldsymbol{B}}_i \otimes \hat{\boldsymbol{C}}_i)^T vec(\mathcal{X}_m)$. Therefore, the core tensor $\hat{\mathcal{G}}_i^{(m)} = \mathcal{X}_m \times_1 \hat{\boldsymbol{A}}_i^T \times_2 \hat{\boldsymbol{B}}_i^T \times_3 \hat{\boldsymbol{C}}_i^T$.

Appendix C

Firstly, rewrite the original objective function in vectorized from as:

$$\underset{vec(\hat{\mathcal{H}}_{ij}^{(v)})}{\operatorname{argmin}} \sum_{v=1}^{N} \|vec(\mathcal{F}_{ijv}) - (\hat{\boldsymbol{A}}_i \otimes \hat{\boldsymbol{B}}_i \otimes \hat{\boldsymbol{c}}_{i_j}) vec(\hat{\mathcal{H}}_{ij}^{(v)})\|^2$$

Since $\mathcal{F}_{ijv}$, $\hat{\boldsymbol{A}}_i$,$\hat{\boldsymbol{B}}_i$ and $\hat{\boldsymbol{c}}_{i_j}$are known, the optimization problem is a typical least square problem. Hence, the closed form solution is: $vec(\hat{\mathcal{H}}_{ij}^{(v)}) = [\hat{\boldsymbol{A}}_i \otimes \hat{\boldsymbol{B}}_i \otimes \hat{\boldsymbol{c}}_{i_j}]^{\dagger} vec(\mathcal{F}_{ijv})$ where $\boldsymbol{M}^{\dagger} = (\boldsymbol{M}^T \boldsymbol{M})^{-1} \boldsymbol{M}^T$.

Appendix D

The frame-wise miss detection rate of the within-layer monitoring was calculated as the fraction of all frames in a test sample where an anomaly was present but not detected, averaged across all the test samples. Similarly, the layer-wise miss detection rate of the between-layer monitoring was calculated as the fraction of all layers in a test sample where an anomaly was present but not detected, averaged across all the test samples. The detailed definition of frame-wise (within-layer monitoring) and layer-wise (between layer-monitoring) miss detection rate can be found in Table II. We summarized the frame-wise and layer-wise miss detection rates for different types of anomalies in Table III, Table IV, and Table V. These results confirm the need to combine process monitoring capabilities at different levels to achieve high anomaly detection performances in the presence of out-of-control states that may occur on different scales.

TABLE II
THE DEFINITION OF MISS DETECTION RATE AT FRAME LEVEL AND LAYER LEVEL

	Miss detection rate	
within-layer monitoring	$\frac{\sum_{i=1}^{N} w_{m_i}}{\sum_{i=1}^{N} W_{m_i}}$ where:	w_{m_i} = number of frames missed out of all the anomalous frames in sample i W_{m_i} = number of anomalous frames in sample i N = total number of test samples
between-layer monitoring	$\frac{\sum_{i=1}^{N} b_{m_i}}{\sum_{i=1}^{N} B_{m_i}}$ where:	b_{m_i} = number of layers missed out of all the anomalous layers in sample i B_{m_i} = number of anomalous layers in sample i N = total number of test samples

TABLE III
THE RESPECTIVE FRAME-WISE AND LAYER-WISE MISS DETECTION RATE OF WITHIN-LAYER AND BETWEEN-LAYER MONITORING STRATEGY FOR THE HOT-SPOT ANOMALY

		Noise factor = 0.05	Noise factor = 0.1	Noise factor = 0.2
within-layer monitoring	Size = 1	0.55	0.90	1
	Size = 2	0.29	0.55	0.84
	Size= 3	0.05	0.19	0.44
between-layer monitoring	Size = 1	1	1	1
	Size = 2	0.56	0.95	1
	Size = 3	0	0.28	0.96

TABLE IV
THE RESPECTIVE FRAME-WISE AND LAYER-WISE MISS DETECTION RATE OF WITHIN-LAYER AND BETWEEN-LAYER MONITORING STRATEGY FOR THE GLOBAL OVERHEATING ANOMALY

		Noise factor = 1	Noise factor = 1.5	Noise factor = 2
within-layer monitoring	offset = 5	0.9998	1	1
	offset = 10	0.9954	0.9995	0.9998
	offset = 15	0.9550	0.9970	0.9999
between-layer monitoring	offset = 5	0	0	0.06
	offset = 10	0	0	0
	offset = 15	0	0	0

TABLE V
THE RESPECTIVE FRAME-WISE AND LAYER-WISE MISS DETECTION RATE OF WITHIN-LAYER AND BETWEEN-LAYER MONITORING STRATEGY FOR THE UNDERHEATING ANOMALY AFFECTING THE WHOLE PART

		Noise factor = 1	Noise factor = 1.5	Noise factor = 2
within-layer monitoring	decrease factor = 0.98	0.9999	0.9999	1
	decrease factor = 0.96	0.9996	0.9999	0.9999
	decrease factor = 0.94	0.9881	0.9985	0.9995
between-layer monitoring	decrease factor = 0.98	0.93	0.98	0.99
	decrease factor = 0.96	0	0.04	0.41
	decrease factor = 0.94	0	0	0

REFERENCES

[1] A. Haleem and M. Javaid, "Additive manufacturing applications in industry 4.0: A review," *Journal of Industrial Integration and Management*, vol. 04, no. 04, p. 1930001, 2019.

[2] W. Yang, J. Chen, K. Paynabar, and C. Zhang, "Identifying the Cyber-Incidents in Additive Manufacturing Systems via Multimedia Signals," in *2020 International Symposium on Flexible Automation*, 07 2020.

[3] R. McCann, M. A. Obeidi, C. Hughes, Éanna McCarthy, D. S. Egan, R. K. Vijayaraghavan, A. M. Joshi, V. Acinas Garzon, D. P. Dowling, P. J. McNally, and D. Brabazon, "In-situ sensing, process monitoring and machine control in laser powder bed fusion: A review," *Additive Manufacturing*, vol. 45, p. 102058, 2021.

[4] M. Grasso, A. Remani, A. Dickins, B. M. Colosimo, and R. K. Leach, "In-situ measurement and monitoring methods for metal powder bed fusion: an updated review," *Measurement Science and Technology*, vol. 32, no. 112001, 2021.

[5] W. Yang, J. Chen, K. Paynabar, and C. Zhang, "Online detection of cyber-incidents in additive manufacturing systems via analyzing multimedia signals," *Quality and Reliability Engineering International*, 2021.

[6] P. Yadav, O. Rigo, C. Arvieu, E. Le Guen, and E. Lacoste, "In situ monitoring systems of the slm process: On the need to develop machine learning models for data processing," *Crystals*, vol. 10, no. 6, 2020.

[7] G. Tapia and A. Elwany, "A review on process monitoring and control in metal-based additive manufacturing." *ASME. J. Manuf. Sci. Eng*, vol. 136, no. 6, 2014.

[8] H. Baumgartl, J. Tomas, R. Buettner, and M. Merkel, "A deep learning-based model for defect detection in laser-powder bed fusion using in-situ thermographic monitoring," *Progress in Additive Manufacturing*, vol. 5, no. 3, pp. 277–285, 2020.

[9] F. Imani, R. Chen, E. Diewald, E. Reutzel, and H. Yang, "Deep learning of variant geometry in layerwise imaging profiles for additive manufacturing quality control," *Journal of Manufacturing Science and Engineering, Transactions of the ASME*, vol. 141, no. 11, 2019.

[10] Z. Yang, Y. Lu, H. Yeung, and S. Krishnamurty, "Investigation of deep learning for real-time melt pool classification in additive manufacturing," vol. 2019-August, 2019, pp. 640–647.

[11] J. Li, L. Cao, J. Xu, S. Wang, and Q. Zhou, "In situ porosity intelligent classification of selective laser melting based on coaxial monitoring and image processing," *Measurement: Journal of the International Measurement Confederation*, vol. 187, 2022.

[12] C. Gobert, E. W. Reutzel, J. Petrich, A. R. Nassar, and S. Phoha, "Application of supervised machine learning for defect detection during metallic powder bed fusion additive manufacturing using high resolution imaging." *Additive Manufacturing*, vol. 21, pp. 517–528, 2018.

[13] I. A. Okaro, S. Jayasinghe, C. Sutcliffe, K. Black, P. Paoletti, and P. L. Green, "Automatic fault detection for laser powder-bed fusion using semi-supervised machine learning," *Additive Manufacturing*, vol. 27, pp. 42–53, 2019.

[14] T. Özel, A. Shaurya, A. Altay, and L. Yang, "Process monitoring of meltpool and spatter for temporal-spatial modeling of laser powder bed fusion process," vol. 74, 2018, pp. 102–106.

[15] H. Yan, M. Grasso, K. Paynabar, and B. M. Colosimo, "Real-time detection of clustered events in video-imaging data with applications to additive manufacturing," *IISE Transactions*, vol. 0, no. 0, pp. 1–28, 2021.

[16] B. M. Colosimo and M. Grasso, "Spatially weighted pca for monitoring video image data with application to additive manufacturing," *Journal of Quality Technology*, vol. 50, no. 4, 2018.

[17] F. M. Megahed, W. H. Woodall, and J. A. Camelio, "A review and perspective on control charting with image data," *Journal of Quality Technology*, vol. 43, no. 2, pp. 83–98, 2011.

[18] K. Paynabar, J. J. Jin, and M. Pacella, "Monitoring and diagnosis of multichannel nonlinear profile variations using uncorrelated multilinear principal component analysis," *IIE Transactions*, vol. 45, no. 11, pp. 1235–1247, 2013.

[19] K. Hu and J. Yuan, "Batch process monitoring with tensor factorization," *Journal of Process Control*, vol. 19, no. 2, pp. 188–296, 2009.

[20] H. Yan, K. Paynabar, and J. Shi, "Image-based process monitoring using low-rank tensor decomposition," *IEEE Transactions on Automation Science and Engineering*, vol. 12, no. 1, pp. 216–227, 2015.

[21] ——, "Real-time monitoring of high-dimensional functional data streams via spatio-temporal smooth sparse decomposition," *Technometrics*, vol. 60, no. 2, pp. 181–197, 2018.

[22] M. Khanzadeh, W. Tian, A. Yadollahi, H. R. Doude, M. A. Tschopp, and L. Bian, "Dual process monitoring of metal-based additive manufacturing using tensor decomposition of thermal image streams," *Additive Manufacturing*, vol. 23, pp. 443–456, 2018.
[23] P. Comon, X. Luciani, and A. L. F. de Almeida, "Tensor decompositions, alternating least squares and other tales," *Journal of Chemometrics*, vol. 23, no. 7-8, pp. 393–405, 2009.
[24] I. Yadroitsev, I. Yadroitsava, and A. D. Plessis, "Basics of laser powder bed fusion," in *Fundamentals of Laser Powder Bed Fusion of Metals*, I. Yadroitsev, I. Yadroitsava, A. D. Plessis, and E. MacDonald, Eds. Amsterdam: Elsevier, 2021, ch. 2, pp. 15–38.
[25] J. MacGregor and T. Kourti, "Statistical process control of multivariate processes," *Control Engineering Practice*, vol. 3, no. 3, pp. 403–414, 1995.
[26] B. L. Welch, "The generalization of 'student's' problem when several different population variances are involved," *Biometrika*, vol. 34, no. 1/2, pp. 28–35, 1947.
[27] A. J. Brockmeier, J. C. Principe, A. H. Phan, and A. Cichocki, "A greedy algorithm for model selection of tensor decompositions," in *2013 IEEE International Conference on Acoustics, Speech and Signal Processing*, 2013, pp. 6113–6117.
[28] B. M. Colosimo, E. Grossi, F. Caltanissetta, and M. Grasso, "A novel prototype for in-situ defect removal in lpbf," *JOM*, vol. 72, p. 1332–1339, 2020.
[29] M. Grasso, V. Laguzza, Q. Semeraro, and B. M. Colosimo, "In-process monitoring of selective laser melting: Spatial detection of defects via image data analysis," *ASME. J. Manuf. Sci. Eng*, vol. 139, no. 5, 2017.